EMBRACE: A Multi-Beam 20,000-Element Radio Astronomical Phased Array Antenna Demonstrator

Gideon W. Kant, Parbhu D. Patel, *Senior Member IEEE*, Stefan J. Wijnholds, *Member IEEE*, Mark Ruiter and Erik van der Wal

***Abstract*—We present the design and development of the Electronic Multi-Beam Radio Astronomy Concept (EMBRACE), a demonstrator that is part of the European contribution towards the Square Kilometre Array, which is currently being designed by the global radio astronomical community. One of the design goals of EMBRACE is to demonstrate the applicability of phased array technology for use in future radio telescopes. The EMBRACE system will ultimately consist of two stations, the largest of which comprises over 20,000 elements and has a physical area of about 160 m^2. The antenna system, covering the 500 – 1500 MHz frequency range, is designed as a dual polarized system, however only the signals for one polarization are processed. To obtain a cost effective design, RF analog beamforming is performed on tile level close to the radiators. The demonstrator is designed to provide two independent beams such that different parts of the sky can be observed simultaneously. First results from part of the array are presented and discussed. The results show that the complete data path is functional. Since the design resembles a large regular contiguous array, all coupling can be taken into account in the embedded element patterns. The array factor therefore suffices to describe the scanning of the array reducing significantly calibration complexity compared to, e.g. sparse, random or more irregular arrays. This is confirmed by the first array factor measurements, that were done using a novel technique that does not require calibration of the array. The first measurements on an astronomical source, the Sun, indicate that the system noise temperature lies between 104 and 118 K, which is reassuringly close to the design target of 100 K.**

***Index Terms*—phased arrays, antenna arrays, array design, mutual coupling, radio astronomy, array signal processing.**

I. Introduction

Since the early 1990s, the global radio astronomy community has been contemplating the design and development of a radio telescope with a sensitivity nearly two orders of magnitudes larger than current instruments. This radio telescope is currently known as the Square Kilometre Array (SKA) [1].

Since its inception in Europe [2]–[5], SKA became a global paradigm and it has evolved in several ways. Important is the increase in frequency range over the years from a possible one band system focusing on the signals from the red shifted 21-cm emission from neutral hydrogen to a multiple band system covering over three decades in frequency. The global community has put forward various antenna concepts to cover parts of the required bandwidth [6]. Over the years, these concepts have been evaluated for their technical merit, ease of manufacturability and the final production and maintainability costs. Presently, only a few key concepts remain which are taken forward for further evaluation through demonstrators [7].

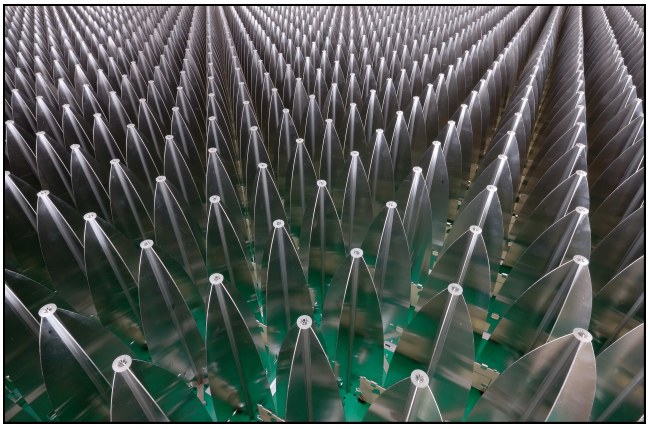

Fig. 1. A picture of the phased array, with aluminum Vivaldi elements in a dual polarization configuration, of one of the EMBRACE stations

A key figure of merit for SKA is the survey speed [8], a measure of how fast SKA will be able to map out a given fraction of the sky with a given sensitivity. The survey speed is proportional to the product of the square of the instantaneous telescope sensitivity and the instantaneous Field-of-View (FoV) of the telescope. The cost per unit survey speed for a given system concept depends strongly on the operating frequency, making distinct system concepts the preferred option for distinct frequency bands.

The instantaneous sensitivity of a radio telescope system is defined by the ratio of its effective area A_{eff} and the system noise temperature T_{sys}. The system noise includes all the noise available from the antenna system as well as the total effective noise of all electronics and losses making up the total receive system. To simplify the following discussion the system noise is decomposed in two parts $T_{\text{sys}} = T_{\text{R}} + T_{\text{sky}}$. Here, the sky noise T_{sky} represents only the signal coming from the direction covered by the main beam. All remaining received noise (from the side lobes of the antenna system), plus the total effective noise of losses and all electronics is denoted as receiver noise T_{R}.

At longer wavelengths (λ), for frequencies $f < 300$ MHz, sky noise temperature is proportional with $\lambda^{2.55}$ [9]. It is thus possible to design a radio telescope system with a system

Manuscript received January 11, 2010. This effort was supported by the European Community Framework Programme 6, Square Kilometre Array Design Studies (SKADS), contract no. 011938.

G. W. Kant, S. J. Wijnholds, M. Ruiter and E. van der Wal are with the R&D Department of ASTRON, Oude Hoogeveensedijk 4, 7971 PD Dwingeloo, The Netherlands (e-mail: kant@astron.nl).

P. D. Patel is with Systems Engineering and Assessment Ltd, Beckington Castle, 17 Castel Corner, Beckington, Somerset, BA11 6TA, UK (e-mail: parbhu.patel@sea.co.uk)

noise dominated by T_{sky} at the lower part of the frequency spectrum. This explains why irregular array configurations with neighboring element distances larger than about a wavelength are popular at these frequencies. Examples of such low frequency arrays having a sensitivity typically dominated by sky noise are the Long Wavelength Array (LWA) [10], [11], the LOw Frequency ARray (LOFAR) [12], [13] and the Murchison Widefield Array [14], [15]. For such arrays, the element gain is more or less constant over a large frequency range, as long as the distance between neighboring elements is larger than about a wavelength. This results in an effective element area proportional to λ^2. This increasing effective area with wavelength, helps compensating the increase in system noise.

At frequencies higher than about 300 MHz, receiving antenna systems looking at the sky, will be dominated by receiver noise, i.e. $T_{\text{sys}} = T_{\text{R}}$. Now a constant $A_{\text{eff}}/T_{\text{sys}}$ can be obtained with a phased array system with neighboring elements distances not much larger than about $\lambda/2$ at the highest operating frequency.

The array design of the Electronic Multi-Beam Radio Astronomy ConcEpt (EMBRACE) comprises a large regular array operating between 500 and 1500 MHz (Fig. 1). A dual polarized array with microstrip fed Vivaldi elements has been designed using the infinite array approach utilizing electromagnetic periodic boundaries.

Somewhere above 1 GHz, it seems clear that the preferred solution for collecting area for SKA appears to be in the form of a reflector with a wide-band feed as suggested by the Technical Demonstrator Program (TDP) [16]. Several options for the feed and optics to be used with the reflector design are being considered [17], [18]. At the lower end of the frequency spectrum, radio astronomy experiments require a large FoV [19]. This makes large reflectors with single pixel feeds less attractive at lower frequencies. One option being considered is to use so called FoV expansion technology. Phased arrays are used as feeds to increase the FoV of reflectors [20]–[22]. However, the application of phased array technology such as demonstrated with EMBRACE, enables features like large independent FoVs, taking radio astronomy instruments even a step further. The concept of phased array antennas is well known in radar, electronic warfare and communications area, however, it represents a paradigm shift in the radio astronomy community. In this paper we describe the design and development of a phased array system, which has been proposed by the Europeans and is endorsed through the SKADS program as their concept towards the SKA radio telescope development [23].

In the remainder of this paper, the design of EMBRACE and the first results are discussed in detail. Section II explains the system level design of the demonstrator telescope and section III provides an overview of the implementation. The detailed design of the phased array antenna demonstrator and its systematic approach to cost reduction, without compromising performance is discussed in section IV. In section V, initial results with measured data from the EMBRACE demonstrator are presented and discussed.

II. System design

In this section the system requirements are given. Furthermore the main architectural design concepts are discussed.

A. System Requirements

The main requirements for EMBRACE are summarized in Table I. The system provides two independent analog beams of approximately 16° beam width at 1 GHz. Both beams are capable of electronically scanning to more than 45° from broadside using a combination of phase shifters and time delay lines. In fact, beams can be scanned to the horizon ignoring the grating lobes at the higher frequencies.

TABLE I
EMBRACE Demonstrator Main Requirements

Requirement	**Remark**	**Value**
Number of stations	In France and the Netherlands	2
Total physical collecting area A_{phy}	Both stations	300 m^2
Aperture efficiency		≥ 0.8
Frequency range		500 – 1500 MHz
System temperature	@ 1 GHz	≤ 100 K
Instantaneous array bandwidth	RF beams	100 MHz
Number of analog beams		2
Polarization	Single linear	1
Half power beam width	RF beam @ 1 GHz	> 15 deg
Scan range θ		≥ 45 deg
Side lobe levels	With respect to main beam. No grating lobes	≤ -13.2 dB
Signal dynamic range	@ output A/D converter	≥ 60 dB
Digital output bandwidth	per analog beam	≥ 40 MHz
Number of digital beams	per analog beam	≥ 8

B. Architecture

In the development phase towards SKA, it is imperative to demonstrate the low cost potential of sufficiently large designs like EMBRACE. Therefore, costs have been a key design driver throughout the design process. An important parameter for the analysis of the required (digital) signal processing, at each point in the system, is the aggregated signal bandwidth. Let b_i represent a signal and $\text{BW}(b_i)$ the bandwidth of that signal. It follows for the aggregated signal bandwidth

$$BW = \sum_{i=1}^{N} \text{BW}(b_i), \tag{1}$$

where N is the number of signals in the system. When the received signals of a radio telescope system like SKA are considered, each signal b_i represents a beam and we denote $\text{FoV}(b_i, f)$ as the FoV of that beam at frequency f. The

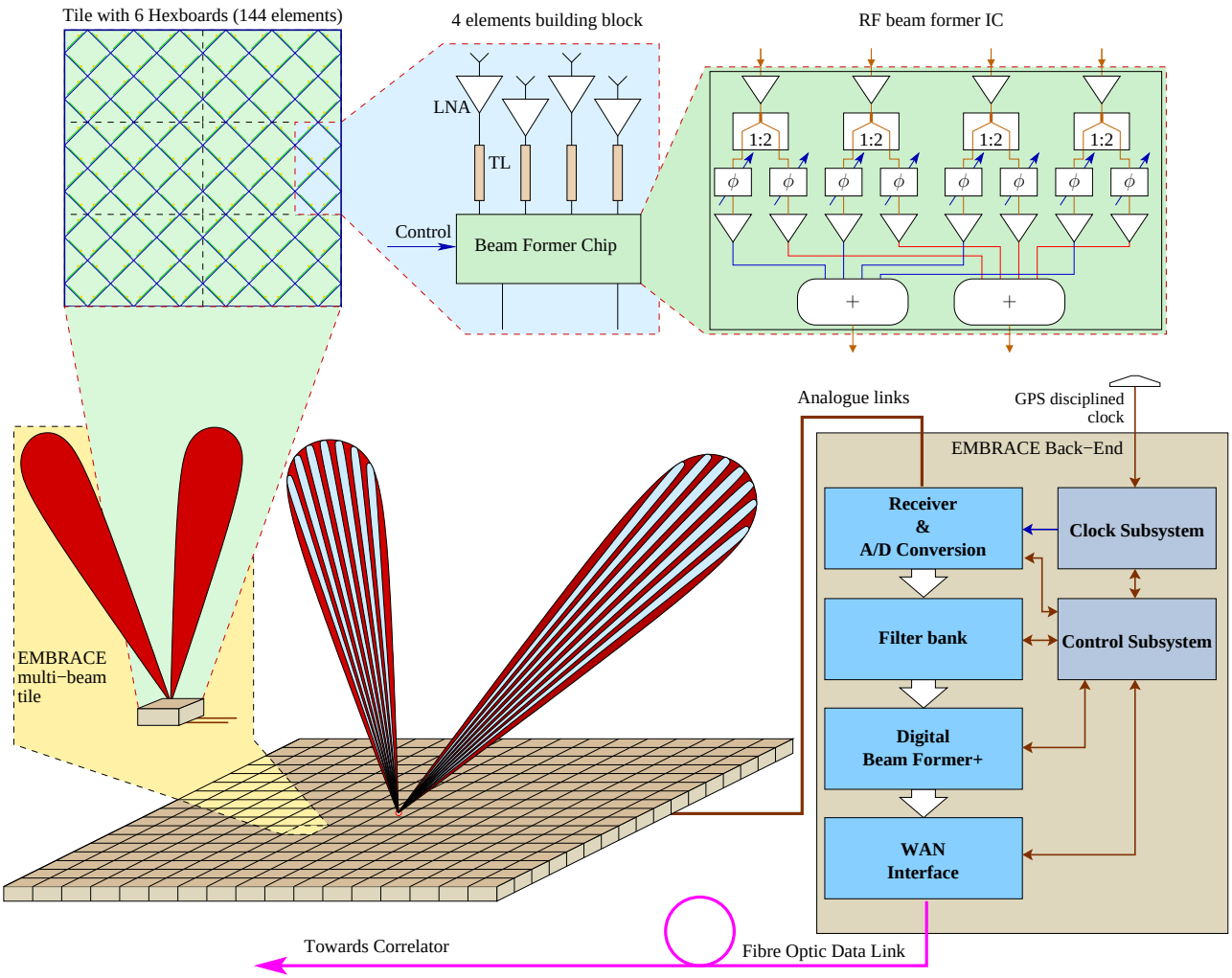

Fig. 2. Block diagram of the EMBRACE station architecture. Antenna signals are combined at tile level using a custom designed beamformer chip. Each tile provides two RF beam signals to a local processing facility, where digital beams are formed. Two coaxial cables transport the RF signals, DC power and control signals to each tile.

aggregated FoV for frequency f follows from summation over all independent beams

$$FoV(f) = \sum_{i \in S} \mathrm{FoV}(b_i, f), \tag{2}$$

where S is the set references of independent beams. When all beams are independent it follows from (1) and (2) that the total bandwidth is proportional with a aggregated FoV. In any case it follows that if more FoV is required at frequency f, more beams are required and therefore more bandwidth needs to be processed. To obtain a cost effective SKA design, the aggregated signal bandwidth needs to match with the processing capabilities at other points in the system. It is of no use to make a large (total) FoV available in the front-end while most of it is discarded further down the system. Future upgrade possibilities should of course be taken into account, but Moore's law will not prevent that the output bandwidth of SKA shall always remain back-end processing limited.

EMBRACE demonstrates how total FoV can be tailored to processing requirements by RF beamforming near the elements to reduce costs. RF beamforming is achieved by organizing the elements in units denoted as tiles. The first beamforming takes place on the elements of a tile. The FoV of a tile beam is defined by the size of a tile.

A system level overview of one EMBRACE station is shown in Fig. 2. An EMBRACE station can be divided roughly into two parts: a front-end and a back-end. The front-end consists of the antenna array including the radome, the supporting mechanics for the array and the signal distribution between the tiles and the back-end. A large phased array system is inherently distributed over a large area. Since active Low Noise Amplifiers (LNAs) have to be integrated close to the elements, the distribution of DC power already forms an important cost driver. In EMBRACE the number of required cables is reduced by multiplexing DC power, control signal and an analog RF beam signal on one coaxial cable (Section III-D).

Whereas the front-end forms a large distributed subsystem by nature, the back-end can be a centralized system (see Section III-C). The back-end handles frequency conversion, analog-to-digital conversion and digital station beamforming. This is an important design choice. Centralizing the analog-to-digital conversion avoids the distribution of additional clock

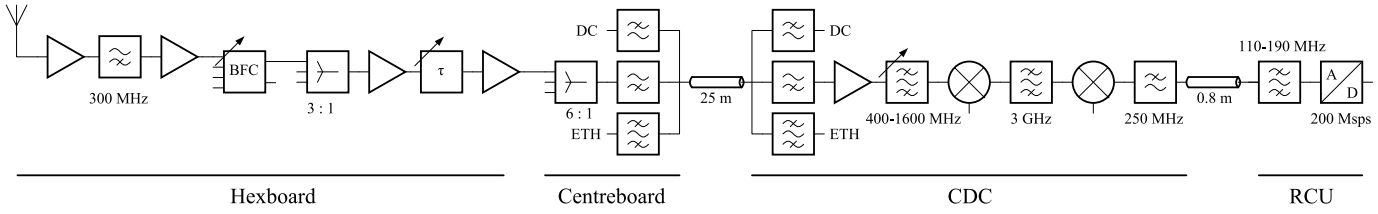

Fig. 3. Block-diagram of the signal path up to the AD converters in the system. Only one signal chain is shown, however points where multiple signals are combined are indicated.

and Local Oscillator (LO) signals towards the tiles. Signal transport between front-end and back-end is implemented with one coaxial link per RF beam per tile. These RF analog links between the tiles and the back-end processing simplifies the tile design and totally decouples the antenna from the receiver. This reduces EMC related problems in general, since the LO and clock signals now have to be distributed in the back-end cabinet only. Furthermore, in the back-end all sensitive analog electronics can be shielded from the digital electronics. A system with analog-to-digital conversion (and frequency conversion if required) in the front-end would not allow for such a clear separation.

The antennas are designed in a dual polarized fashion, however the signals from only one polarization are electronically processed. This setup includes all electromagnetic effects of a dual polarized configuration. From a technical point of view the step to build a front-end, capable to process two polarizations, is just a matter of doubling the front-end electronics with respect to one polarization.

C. Beam Steering

Beam steering in phased array systems is based on the concept of compensating the difference in time of arrival on each antenna for a wave front. This compensation can be implemented using delay lines or phase shifters. Delay lines and phase shifters each have their benefits. Within EMBRACE the main considerations were bandwidth and the possibilities for integration. Delay lines are perfect for bandwidth, but are hard to integrate in an RFIC/MMIC, either limited by noise (RC networks) or physical dimensions (LC networks or pure true time delays). Phase shifters can be relatively easily integrated, but have bandwidth limitations on a system level, even if an ideal phase shifter was designed. The problem arises due to the fact, that a phase shift can only approximate a time delay over a small frequency range ($\tau = -\varphi/\omega$). Over larger frequency ranges, the beam will start to squint.

EMBRACE uses a hybrid approach, to combine the best of both worlds. In the first combination steps only phase shifters are used. In this stage we still have a broad beam width, so squint does not cause significant gain loss. For the subsequent combination step, a true time delay can be selected to reduce the gain loss caused by beam squint.

After combining 72 antennas, the signal is digitized and further beamforming is performed by splitting the frequency range into subbands. Each subband is sufficiently small, to allow for phase shifting in the digital domain. The resulting digital beam can be scanned with almost arbitrarily small steps as a result of the 16 bit digital beamformer coefficients.

D. System Dynamic Range

The dynamic range of the system is determined by two factors. At the low end, it is limited by noise. At the high end, the system is limited by linearity of the components.

The system noise figure is determined by several factors. It is a summation of noise contributions starting at the antenna enclosure, the resistive losses of the antenna element, the total front-end up to the A/D converter. Its main contribution is primarily dominated by the first stage in the front-end, the LNA.

There is compromise between linearity and system noise figure. More gain in the systems improves the noise figure, but it degrades the linearity of the system. The EMBRACE locations at both Westerbork and Nançay are not Radio Frequency Interference (RFI) quiet regions. Broadband systems such as EMBRACE have to cope with the RFI in the received frequency band. This results in strong linearity requirements. Increasing linearity of the active devices results in considerable additional power consumption and dissipation issues.

Looking at the noise contributions of the EMBRACE system, it is interesting to note that from the total noise figure, 67 % is accounted to the first LNA. Other large noise contributions are the antenna element (10 %) and second stage amplifier (7 %). The remaining 16 % is contributed by the rest of the RF chain.

It is well understood that the noise figure of an LNA is dependent on the source impedance of the antenna [24]. This can be described by

$$F = F_{\text{min}} + 4r_{\text{n}} \frac{\left|\Gamma_{\text{src}} - \Gamma_{\text{opt}}\right|^2}{\left(1 - \left|\Gamma_{\text{src}}\right|^2\right)\left|1 + \Gamma_{\text{opt}}\right|^2}, \tag{3}$$

where F_{min} is the minimal noise figure, r_{n} is the normalized noise resistance, Γ_{src} is the source impedance and Γ_{opt} is the optimum noise impedance. The source impedance for array systems should not be the (passive) impedance of the antenna. It has been shown that in case of array systems, the active impedance of the array is of importance. The active reflection coefficient of element i can be written as [25]

$$\Gamma_{\text{act},i} = \frac{1}{w_i} \sum_{j=1}^{N} w_j S_{\text{ant},j,i}\big|_{Z_0 = Z_{\text{LNA}}}, \tag{4}$$

where w_i is the complex weight of each channel and S_{ant} contains the coupling matrix between all antenna elements.

Since each beam direction has a unique set of weights, the active reflection coefficient depends on beam steering and thus the noise figure of the system will be influenced by beam steering. So for a low noise phased array system, not only F_{min} has to be considered. Both the active reflection coefficient and r_{n} should deserve equal, if not more attention.

III. System Implementation

In this section, implementation details are discussed per subsystems. The discussion starts at the radome following the signal path to the back-end as shown in Fig 3.

A. Radome

To protect the electronics from the outside environment, such as sun, wind, rain and snow, a radome is needed. The total size is (L×W×H) 17 m×15 m×4.2 m for a station. The physical area of the array is 162 m^2. Extra space is incorporated in the radome to allow for some working space around the array.

The radome should be capable of handling extreme weather conditions in the Netherlands, 0.5 m of snow and wind speeds up to 12 Beaufort. Furthermore, it also provides a thermal barrier to prevent thermal shocks.

These mechanical requirements are generally not compliant with the desired behavior for radio observations. A radio 'transparent' enclosure is required and no obstructions are allowed within the scan range. A good low cost material choice in combination with clever structural solutions, combine the aforementioned requirements. Electrical properties of the materials have been verified by using an high-Q waveguide cavity (TE110-mode), filled with the material. Both dielectric constant and dissipation factor showed excellent RF behavior.

A measurement campaign has been performed at the Westerbork Synthesis Radio Telescope (WSRT) site, to assess the RFI situation. This showed that the most dominant RFI sources originate from a single location: A 300 m high broadcast tower, at approximately 10 km distance. The fact that most RFI comes from a single location, can be used to our benefit. Since the antenna pattern has a null at the horizon in the H-plane, the elements are oriented such that the null is directed towards the television tower to suppress the RFI. Since the radome orientation is coupled to the antenna rotation, its orientation is also set.

B. Tile

Each tile consists of six identical hex boards and one center board, as shown in Fig. 4. A hex board has 24 Vivaldi antenna elements. The linearly polarized Vivaldi antennas of the array are fabricated from inexpensive folded sheets of aluminum. Since only one polarization is used, the signals from only 12 elements are amplified. The 72 elements of one polarization with an element spacing of 12.5 cm result in a square tile of $72 \times (0.125 \text{ m})^2 = 1.125 \text{ m}^2$. More details on the antenna array design are given in section IV.

From (3) it is evident that both the active reflection coefficient and r_{n} play a key role in wide-band noise optimization.

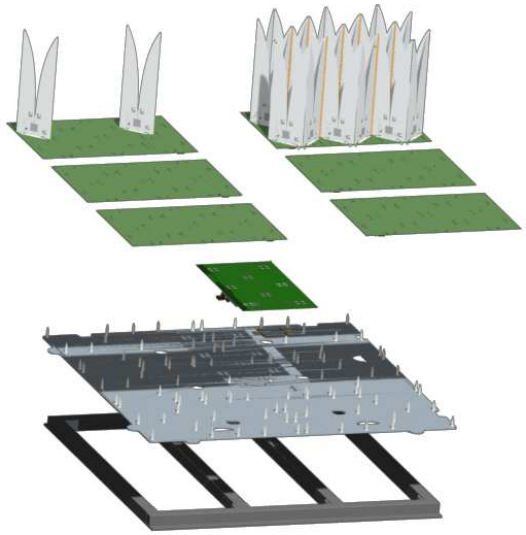

Fig. 4. Exploded view of a single EMBRACE tile, showing antenna elements, hex boards and center board as well as mechanical support frames

The r_{n} is dominated by the transistor itself. A market survey of transistors, that combine a low r_{n} in combination with a low F_{min} and reasonable matching, resulted in one of Avago's E-pHEMT devices. Any components between the LNA and the antenna terminal will either limit the bandwidth or increase the noise. The solution was found by selecting a suitable source impedance target. An impedance of about 70 Ω proved to be a good compromise between noise behavior, reflection, stability and manufacturability. After amplification of the signal by the first stage, a high pass filter is included to remove the lower part of the spectrum. A second stage delivers the signal to the beamformer chip. Each beamformer chip combines the signals from four elements into two independent outputs. Beams are defined by introducing proper phase shifts to each input signal. To create the phase shifts, the design uses a vector modulator approach, with a filter network generating the four main phase states 0, 90, 180 and 270 degrees. Smaller phase steps can be created by combining these vectors.

Since the RF beamformer function is essential to achieve the required cost reduction, a dedicated chip has been developed using the QUBIC4G BiCMOS 0.25 μm SiGe technology from NXP. The chip provides amplitude control to compensate for gain variation. The amplitude and phase states can be selected through a serial interface.

At the output of the beamformer chip, the two resulting beam signals are further processed in two independent equal signal chains. Only a single chain is shown in Fig. 3. After combining the corresponding signals of each beam, the signal is amplified and a delay line (one bit) can be selected.

On the center board the signals coming from the six hex boards are combined and the two resulting beam signals are transported over two coaxial cables to the back-end. The same coaxial cables are used for transporting DC power and Ethernet control signals. The center board provides the functionality for (de-)multiplexing the three signals and further processing and distribution of the DC power and control signals to the hex boards.

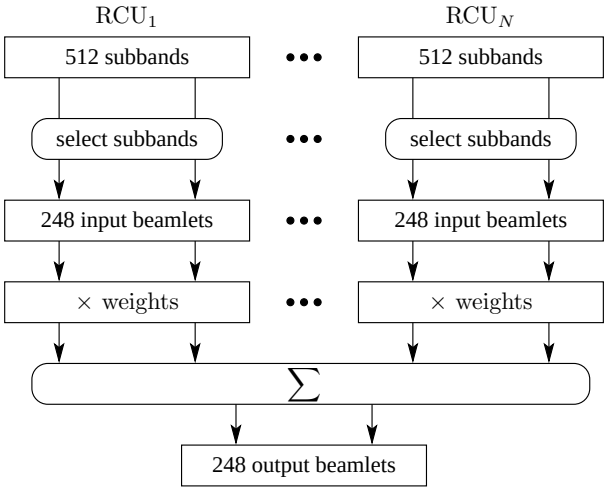

Fig. 5. The digital beam former architecture

C. Back-end

The back-end contains all the remaining electronics required for processing the signals from the tiles including the control subsystem. First, the beam signals are down converted and digitized. In the digital domain, the signal is represented as a series of narrow band signals and digital beams are formed. The back-end part is hosted in a small shielded shelter near the array. The back-end is depicted at the right hand side in Fig. 2.

The Control and Down Conversion (CDC) board provides an Ethernet control interface, an interface for DC power distribution and functionality for converting a selected RF band down to a (low) IF frequency (center frequency 150 MHz) suitable for digitization. The RF conversion uses a superheterodyne mixing scheme. A 3 GHz intermediate frequency has been chosen to create enough spectral distance for image suppression using a 100 MHz wide band pass filter. A second mixer stage converts the signal down to a low IF with a center frequency of 150 MHz.

The IF signal is fed into the Receiver Unit (RCU). The analog signal is further bandpass limited with an anti-aliasing filter and finally converted to the digital domain by a 12-bit 200 MS/s A/D converter. The conversion is done from the second Nyquist zone and the effective input frequency range is from about 110 to 190 MHz.

TABLE II
EMBRACE BANDWIDTH OVERVIEW

Point in system	N	$\mathrm{BW}(b_i)$	$\mathrm{FoV}(b_i, f = 1\ \mathrm{GHz})$
Output LNA	72×144	≥ 1 GHz	π sr
Output Tile	2×144	200 MHz	0.061 sr
Input ADC	2×144	100 MHz	0.061 sr
Output Station	2×248	195 kHz	0.00031 sr

The digital beamforming architecture is depicted in Fig. 5. First the digital signal is converted into a series of 512 subbands by using a polyphase filter bank. Each subband is complex sampled and therefore the sample frequency is decimated by 1024. A maximum of 248 subbands can be selected for multiplication with complex valued weights. The resulting output signals (denoted as beamlets) are added. For each resulting beamlet the frequency and weighting can be chosen individually. In table II an overview of bandwidth and FoV at several points in the system are given using the terminology as discussed in Section II-B. From the table it may be concluded that the processing bandwidth is not well balanced throughout an EMBRACE station. However, the main focus in EMBRACE was on the front-end and it was allowed for being limited by the back-end processing.

D. Array Control and Supply Implementation

Each tile can be controlled independently using raw Ethernet frames. The point-to-point communication is interfaced to one of the two coaxes that connect the tile to the CDC board in the back-end. The CDC provides a standard RJ-45 connector and the Ethernet signal is interfaced through active circulators at both ends. In the back-end, standard Ethernet switch equipment is used to connect all tiles to a control computer. A tile only responds to incoming messages i.e., it does not initiate communication. The control signal uses the 10 Mb/s signaling scheme thus filling the lower part of the spectrum below the spectrum of the beam signal on the coax. The separation of control and beam signal is ensured by multiplexing and de-multiplexing filters at both ends.

A phantom supply architecture is selected to distribute 48 V DC power to the tiles. Due to limited current capability of the cables and connectors a high voltage has been chosen and the current is distributed over both coaxial cables. Additional filtering is implemented on the CDC back plane to reduce spurious signals coming from the power supplies.

IV. Antenna Array

A. Design Approach

Since 1995, an R&D program has been conducted at ASTRON regarding wide band aperture array technology for the SKA. A range of demonstrators have been developed and the precursor of EMBRACE was the Thousand Element Array (THEA) [26]–[29]. With THEA, a wide band phased array based on Vivaldi radiators was successfully demonstrated [30]. Therefore, the Vivaldi radiator was again chosen as the appropriate radiator to produce a scanning array over a bandwidth of greater than 3:1 ratio.

As the demonstrator stations will be large phased arrays ($\geq 20\lambda \times 20\lambda$), it is appropriate to design it using an infinite array approach. A Periodic Boundary Finite Difference Time Domain (PB-FDTD) code, developed in [31], has been used in the design of the array. It is known to give accurate results on Vivaldi arrays, has been extensively used elsewhere and is known to produce excellent results [32].

The general target array design parameters are given in table III. The design of a phased array starts with the scanning requirement at the highest frequency of operation. This provides the element separation, producing a radiation pattern free of grating lobes within the visible range. An analog RF beam follows from the combination of the elements of one tile. The FoV of the resulting RF beam is inversely

TABLE III
TARGET DESIGN PARAMETERS FOR THE EMBRACE PHASED ARRAY ANTENNA.

Parameter	**Target value**
Frequency range	400 – 1600 MHz
Half power RF beam width @ 1 GHz	> 15 deg
Scan range θ	≥ 45 deg
Side lobe levels With respect to main beam.	≤ -13.2 dB
Grating lobes	None
Reference impedance	70 Ω
VSWR (active reflection)	≤ 2

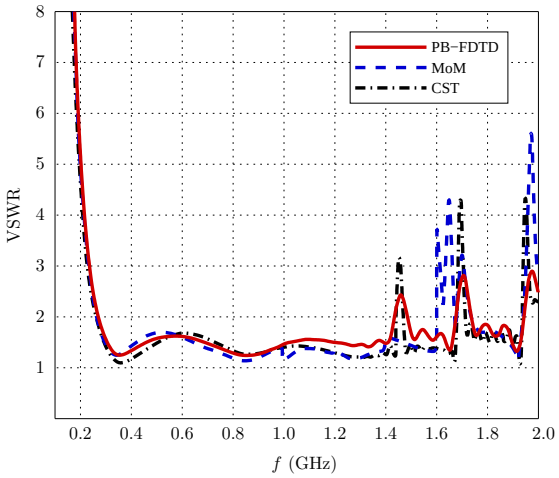

Fig. 6. VSWR versus frequency simulations at broadside of the first bilateral prototype array

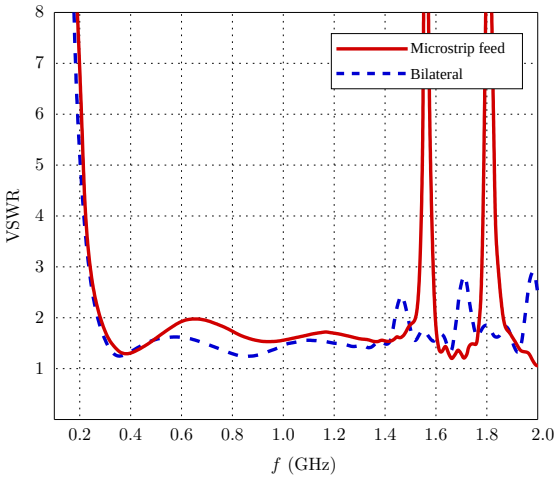

Fig. 7. VSWR versus frequency simulations of an aluminum Vivaldi array fed by a microstrip feed compared with the original bilateral Vivaldi design.

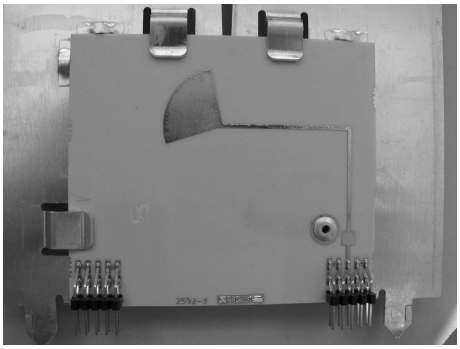

Fig. 8. Close up of the final feed arrangement on the radiator. A rivet in combination with alignment features and clips are used to fixate the board.

proportional with the size of the tile. A beam width of about 15 degrees at $f = 1$ GHz on tile level was set as a requirement demonstrating a relatively large FoV.

It follows that with an element separation of 12.5 cm, an 8×8 element array can meet the scanning requirement up to 45 degrees at $f = 1.4$ GHz in combination with the FoV requirement. A first single polarization prototype was designed using Vivaldi elements with stripline feeds on FR4 material. The Vivaldi array was optimized using the PB-FDTD code and the results were verified using several other codes.

In Fig. 6, voltage standing wave ratio (VSWR) simulation results are shown as function of frequency obtained with PB-FDTD, Method of Moments code from [33] and commercially available EM software from CST. It is clear that there is a high degree of correlation in the results.

B. Final Prototype

The first array prototype design had two major drawbacks. Losses in the FR4 dielectric were too high to meet the noise requirement and the first array prototype was a single polarization design. Going to more expensive microwave material for the complete element would render an implementation out of cost bounds, so this was not option. To overcome this issue, the design of the tile is changed by replacing the FR4 elements with a radiator made of a solid but fairly thin sheet of aluminum. The aluminum radiator is excited with a microstrip feed designed using Rogers 4003 material ($\varepsilon_r = 3.38$) which, although made very small, is still the most costly item on the antenna and hence there may be further opportunities for cost reduction. As the microstrip line on the feed board is in front of the LNA, such low loss substrate is essential to meet the noise requirements.

Furthermore the step was made from a single polarization setup to a dual polarized configuration. Analysis with the PB-FDTD code showed that both the linearly and dual polarized antennas are easily achievable with a very similar reflection coefficient versus frequency curve. The cost and the long term effects of the material have been taken into consideration. Although EMBRACE requires a linearly polarized array only, the electromagnetic design is dual polarized.

In Fig. 7, the VSWR is shown of an aluminum radiator model with microstrip feed. It resembles closely the results obtained for the bilateral Vivaldi with a stripline feed.

A detailed arrangement of the feed on the radiator is shown in Fig. 8, where the alignment features and clips to hold the feed in place are clearly visible. The feed board is fixed on the radiator by means of a rivet. With the arrangement of Vivaldi radiators made out of thin but solid aluminum sheets and microstrip feeds on a Rogers 4003 material, the

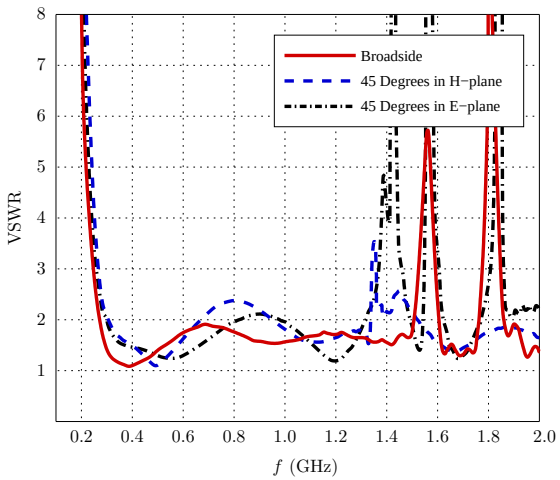

Fig. 9. VSWR vs. frequency simulations at broadside and 45 degrees in H and E Planes of a dual polarized array modeled with assembly holes.

design was considered to be fairly close to optimum in terms of cost and performance for the demonstrator. An extensive analysis on the behavior of the active reflection coefficient of an element for broadside and several scan directions was therefore carried out on this particular configuration of the feed and radiator. This included the effects of the assembly holes in the radiators. The results shown in Fig. 9, including assembly details, still resemble quite well with the previous results obtained from the linearly polarized case. Resonances appear at 1.4 GHz when the array is scanned to 45 degrees along the cardinal planes (E and H plane). However, when scanning the beam a few degrees away (towards zenith or away from the cardinal planes), these resonances dissappear. A prototype tile based on this dual polarized aluminum Vivaldi array has been built and evaluated. First measurements on the VSWR pattern confirmed the simulation results on maximum VSWR. However the specific shape of the measured pattern was not predicted by the simulations. The differences are subject of an ongoing study.

C. Final Array Design

As mentioned in Sec. II, the demonstrator array is organized in tiles. The array is designed using infinite array assumptions. We have therefore chosen to maintain electrical continuity between the tiles. In order to achieve this continuity in practice, the radiating elements on the final tile design were oriented at 45 degrees angles with the tile edges. The final tile design contains 2×72 antenna elements and its final size is 1.125 m^2. A picture of the final tile is shown in Fig. 10. The mechanical design of the radiator has also evolved one step further. In the final design single, radiator elements are connected together using extruded profiles between the elements.

The final antenna and feed geometries with dimensions are shown below in resp. Fig. 11, Fig. 12, Table IV and Table V.

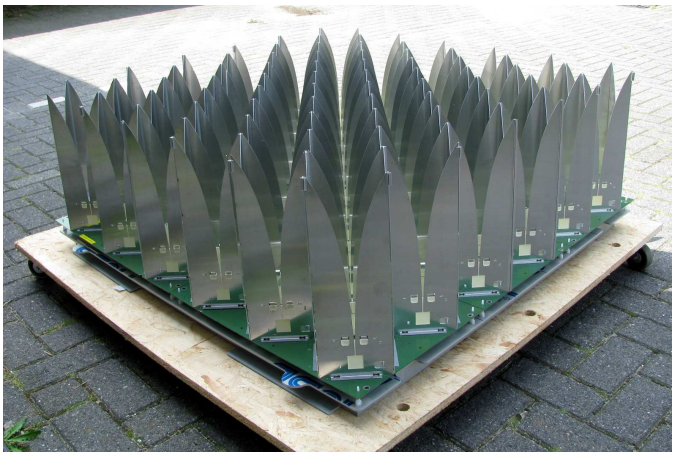

Fig. 10. An EMBRACE tile of the final design with aluminum Vivaldi radiators in a dual polarization configuration.

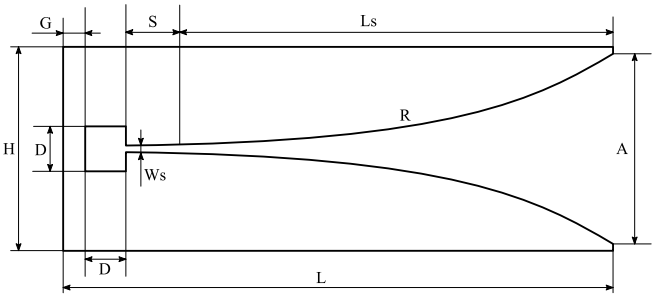

Fig. 11. Final antenna geometry

TABLE IV
FINAL ANTENNA DIMENSIONS.

Antenna dimensions	**Value**
Element Separation (H)	124 mm
Aperture Height (A)	118 mm
Tapered Slot Length (Ls)	294 mm
Rate of Exponential Slotline (R)	0.01 mm^{-1}
Cavity Length (D)	26 mm
Slotline Width (Ws)	2 mm
Constant Slotline Length (S)	15 mm
Cavity Ground Distance (G)	15 mm
Total Antenna Length (L)	350 mm

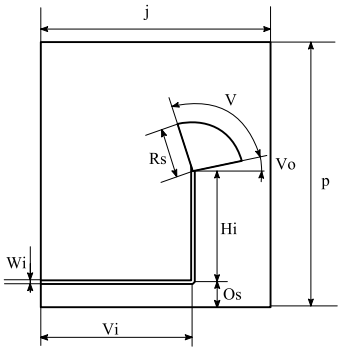

Fig. 12. Final feed geometry

TABLE V
FINAL FEED BOARD DIMENSIONS.

Feed Dimensions	Value
Stripline Width (Wl)	1 mm
Stub Radius (Rs)	15 mm
Stub Opening Angle (V)	96°
Stub Outer Angle (Vo)	12°
Board Width (p)	82 mm
Board Length (j)	70 mm

V. INITIAL RESULTS

A. Coordinate Systems

In the antenna design and testing community, it is common to express observation directions using the angles (θ, ϕ) or the associated direction cosines (u, v, w). These coordinate systems are fixed to the antenna system instead of to the Earth or the sky, which makes them less suitable for radio astronomical applications. Moreover, (u, v, w)-coordinates are commonly used in radio astronomy to describe the baseline vectors between pairs of antenna elements in an array. In radio astronomy, positions on the sky are therefore expressed in azimuth, az, measured from North (0°) through East (90°), and elevation, el, measured from the horizon (0°) positive towards zenith (90°). The associated direction cosines are referred to as (l, m)-coordinates and defined such that l points East and m points North, i.e.

$$l = \sin(az)\cos(el), \quad (5)$$

$$m = \cos(az)\cos(el). \quad (6)$$

Since phased arrays suffer from projection effects when steered away from broadside, these direction cosines turn out to be highly convenient for phased arrays placed in the local horizon plane.

B. Data Model

The signals received by the K antennas in the pth tile can be described by a superposition of Q source signals $s_q(t)$, each source signal being attenuated by the direction dependent gain g_{pkq} depending on the matching between the element pattern of the kth antenna and the qth incident wave. The analog beamformer in the tile applies a phase rotation $w_k = \mathrm{e}^{\mathrm{j}\phi_k}$ to steer the tile beam to the desired direction. The output signal of the pth tile can thus be described as

$$y_p(t) = \sum_{k=1}^{K} w_k \left(\sum_{q=1}^{Q} g_{pkq} \mathrm{e}^{\mathrm{j}\mathbf{k}_q \cdot \boldsymbol{\xi}_{pk}} s_q(t) + n_{pk}(t) \right), \quad (7)$$

where $n_{pk}(t)$ is the noise signal from the antenna and LNA and $\mathrm{e}^{\mathrm{j}\mathbf{k}_q \cdot \boldsymbol{\xi}_{pk}}$ describes the propagation delay over the array by a phase rotation at the observing frequency by the wave propagation vector $\mathbf{k}_q$ and the antenna position $\boldsymbol{\xi}_{pk}$.

Since the measurements presented in this paper were done with a single dominant source, we specialize to $Q = 1$ for notational convenience. We can then define the gain of the tile beam pattern g_{0p} towards the source as $g_{0p} = \sum_{k=1}^{K} w_k g_{pk} \mathrm{e}^{\mathrm{j}\mathbf{k}\cdot\boldsymbol{\xi}_{pk}}$ and the tile noise signal as $n_{0p}(t) = \sum_{k=1}^{K} w_k n_{pk}(t)$. This simplifies the output signal of the pth tile to

$$y_p(t) = g_{0p} s(t) + n_{0p}(t). \quad (8)$$

The output signal of the pth RCU depends on $y_p(t)$, the direction independent complex valued receiver path gain g_p and the noise added by the receiver channel electronics $n_{rp}(t)$. The output signal of the pth RCU can therefore be described as

$$x_p(t) = g_p g_{0p} s(t) + n_p(t), \quad (9)$$

where $n_p(t) = g_p n_{0p}(t) + n_{rp}(t)$.

The on-site FPGA-based digital signal processing boards can real-time correlate the signals from all RCUs for one subband. The result can be integrated over an integral multiple of one second before it is stored on a local hard disk. We will refer to such a measurement as a snapshot or short term integration. If we denote the nth sample of the pth RCU by $x_p(nT)$, where $T = 5.12$ μs is the sampling period of a Nyquist sampled subband signal, and stack them in the $P \times 1$ array signal vector $\mathbf{x}(nT) = [x_1(nT), x_2(nT), \cdots, x_P(nT)]^T$, the measured array covariance matrix produced by the on-site digital processing in a short term integration is given by

$$\widehat{\mathbf{R}} = \sum_{n=1}^{N} \mathbf{x}(nT)\, \mathbf{x}^H(nT). \quad (10)$$

We can stack the receiver path gains in a $P \times 1$ vector $\mathbf{g} = [g_1, g_2, \cdots, g_P]^T$ and the noise signals in a $P \times 1$ noise vector $\mathbf{n}(t) = [n_1(t), n_2(t), \cdots, n_P(t)]^T$. Defining the diagonal matrix $\mathbf{G} = \mathrm{diag}(\mathbf{g})$ and assuming that the tile beam patterns are the same, i.e., that all tiles are steered in the same direction and they have the same electromagnetic response, we can model the array signal vector as

$$\mathbf{x}(t) = \mathbf{G}\mathbf{a} g_0 s(t) + \mathbf{n}(t), \quad (11)$$

where $\mathbf{a} = \left[\mathrm{e}^{\mathrm{j}\mathbf{k}\cdot\boldsymbol{\xi}_1}, \mathrm{e}^{\mathrm{j}\mathbf{k}\cdot\boldsymbol{\xi}_2}, \cdots, \mathrm{e}^{\mathrm{j}\mathbf{k}\cdot\boldsymbol{\xi}_P}\right]^T$ is the array response vector describing the propagation delay over the array of tiles.

We will assume that the source signal is not correlated with the noise signals and that the noise signals of the individual receiver channels are uncorrelated, but have the same power. The data model for the array covariance matrix then becomes

$$\begin{aligned} \mathbf{R} &= \mathcal{E}\left\{\mathbf{x}(t)\,\mathbf{x}^H(t)\right\} \\ &= \mathbf{G}\mathbf{a} g_0 \sigma \overline{g_0} \mathbf{a}^H \mathbf{G}^H + \sigma_n \mathbf{I}, \end{aligned} \quad (12)$$

where $\sigma = \mathcal{E}\{s(t)\,\overline{s}(t)\}$ is the source power, σ_n is the system noise power and $\mathbf{I}$ is the identity matrix. Since σ and g_{0p} are both scalars, they commute and we can therefore define the gain of the tile power beam pattern as $\gamma = g_0 \overline{g}_0 = |g_0|^2$.

C. Tile Beamformer Validation

Since the source model $\mathbf{G}\mathbf{a}\gamma\sigma\mathbf{a}^H\mathbf{G}^H$ has rank one, an Eigenvalue decomposition on $\mathbf{R}$ will yield a dominant Eigenvalue

$$\lambda_1 = \|\mathbf{G}\mathbf{a}\|^2 \gamma\sigma + \sigma_n \quad (13)$$

with dominant Eigenvector

$$\mathbf{v} = \mathbf{G}\mathbf{a} / \|\mathbf{G}\mathbf{a}\|, \quad (14)$$

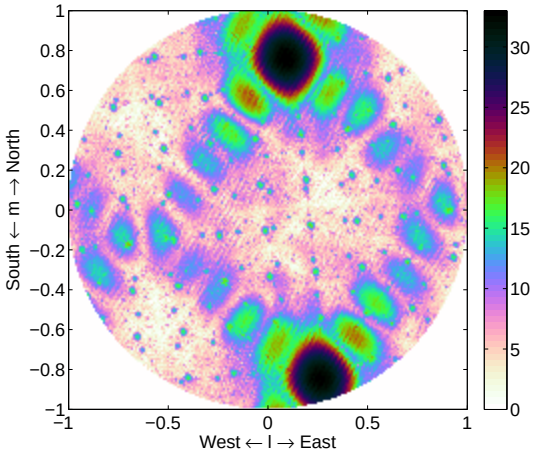

Fig. 13. Plot of the SNR measurement on the geostationary satellite Afristar at 1475.25 MHz obtained from (15) showing the average array factor towards Afristar of 9 tiles arranged in a 3×3 uniform rectangular array while scanning over the entire sky.

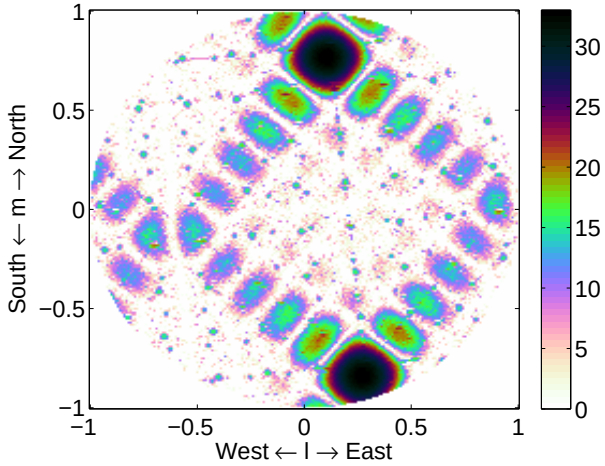

Fig. 14. Simulated array factor towards Afristar when the tile beam is scanned over the sky taking into account the round-off errors of the 3-bit analog beamformer. This closely matches the measured array factor shown in Fig. 13 indicating that the tile beamformer works as expected.

while all other Eigenvalues are equal to the noise power σ_n. If we steer the tile in the direction (θ, ϕ) and perform an Eigenvalue decomposition on the measured array covariance matrix $\widehat{\mathbf{R}}$, we can thus compute

$$\frac{\widehat{\lambda}_1 - \frac{\sum_{p=2}^{P} \widehat{\lambda}_p}{P-1}}{\sum_{p=2}^{P} \widehat{\lambda}_p / (P-1)} = \frac{\|\mathbf{Ga}\|^2 \widehat{\gamma}(\theta,\phi)\,\sigma}{\sigma_n} = \frac{\|\mathbf{Ga}\|^2 \sigma}{\sigma_n} \widehat{\gamma}(\theta,\phi)\,. \tag{15}$$

Assuming that the receiver path gains and the propagation delays towards the source are constant over the observation, $\|\mathbf{Ga}\|$ is constant over the measurement and we can use the SNR derived from (15) to probe the tile power beam pattern $\gamma(\theta,\phi)$ towards the source while pointing the tile in the direction (θ,ϕ).

Since $\gamma(\theta,\phi)$ is given by

$$\gamma(\theta,\phi) = \left| \sum_{k=1}^{K} w_k(\theta,\phi)\, g_p e^{j\mathbf{k}\cdot\boldsymbol{\xi}_{pk}} \right|^2, \tag{16}$$

this SNR measurement allows us to probe the array factor towards Afristar while the analog tile beamformer is scanned over the sky assuming that all tiles behave identically. Such an experiment was done with a uniform rectangular sub-array of 3×3 tiles at 1475.25 MHz using the geostationary satellite Afristar located at $(az, el) = (162.16, 28.07)$. In this experiment, the tiles were scanned over a regular grid in the (l, m)-plane with 0.01 resolution defined in such a way that Afristar was exactly on a grid point.

For each point in the scan, the digital processing back-end was used to produce a snapshot covariance matrix integrated over 1 s. Equation (15) was used to obtain the SNR of Afristar for each pointing. The result is shown in Fig. 13. This image shows Afristar close to the Southern horizon and its grating lobe to the Northern horizon.

This side lobe and grating lobe pattern can easily be explained by the array factor of a single tile. Each tile can be considered a 6×6 uniform rectangular array of square unit cells each consisting of two antenna elements as shown

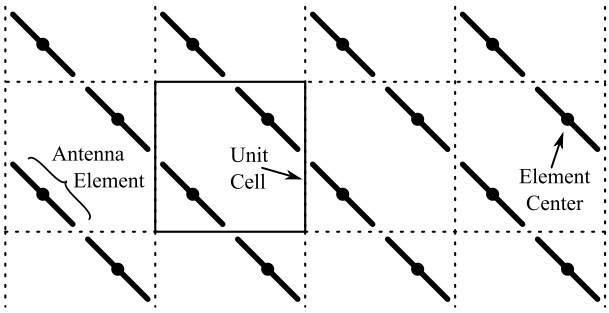

Fig. 15. Unit cell to explain the side lobe pattern in Fig. 14.

in Fig. 15. The combination of the array factor of the 36 unit cells and the 6×6 uniform rectangular grid gives the measured array factor pattern. This pattern is distorted by a regular array of sharp peaks at about 17 dB on a regular grid with about 0.2 spacing that is aligned with the orientation of the tiles. This pattern is produced by round-off errors in the 3-bit phase rotations in the analog beamformer. The complete pattern can be reproduced exactly in simulation as demonstrated by Fig. 14. From these experiments we conclude that the tile beamformers are working properly and that we have an accurate model to predict its behavior.

D. Scanning with Multiple Tiles

The advantage of correlation over beamforming is, that we can apply different beamforming schemes and produce images with and without calibration. We can also increase the resolution in the image demonstrating that an all sky map may be produced by mosaicing.

The image shown in Fig. 16 was obtained by making sub-images of 5×5 pixels around each pointing from the measurement described in the previous section increasing the resolution to 0.002. The phase calibration was done on the single 1 s snapshot on Afristar. Since Afristar is the single dominant source on the sky, we can follow the approach used in [34] to calibrate LOFAR's initial test station on an RFI

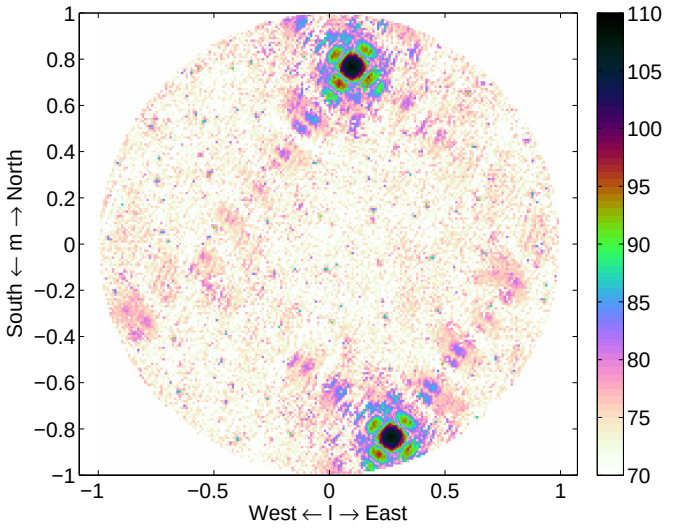

Fig. 16. All sky scan at 1475.25 MHz with a 3×3 uniform rectangular array of tiles. The scan resolution was improved from 0.01 to 0.002 by deriving 5×5 sub-images from the measured covariance matrix at each grid point.

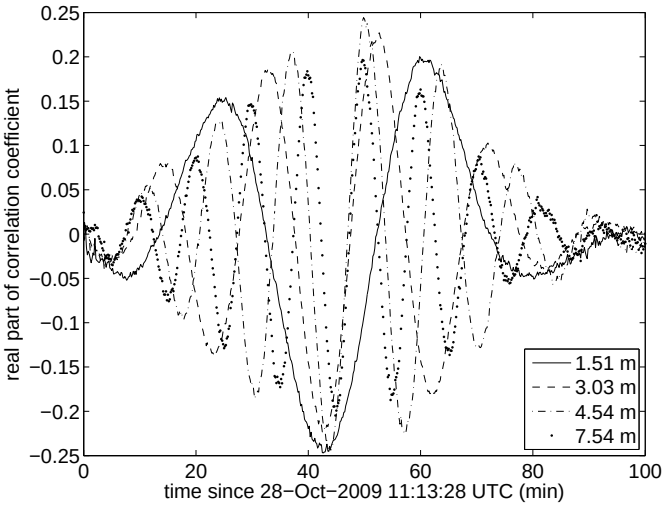

Fig. 17. Plot showing fringes on the sun on a number of baselines with the indicated lengths from a 6-element ULA. The observation was done in a single 195 kHz frequency channel at 1179 MHz with 10 s integration per sample.

source, i.e., compute

$$\mathbf{g}\mathbf{g}^H = \widehat{\mathbf{R}} \oslash \left(\mathbf{a}\mathbf{a}^H \gamma\sigma\right), \tag{17}$$

where $\oslash$ denotes the element-wise division of two matrices and obtain $\mathbf{g}$ from an Eigenvalue decomposition. This calibration method is a specialization of the more general approach discussed in [35] that generally works well for calibration on a single strong source. The obtained gain vector was only used for phase calibration. The amplitude calibration was done separately for each pointing by applying the same technique to each snapshot but only using that information to correct amplitude differences. In principle, Afristar is sufficiently strong to obtain a phase correction as well, but is likely to produce phase ambiguities due to the coarse sampling: the centroids of the tile are separated by 1.06 m, while the observed wavelength is 0.203 m.

Although the calibration can be improved further by regularly repeating the calibration on Afristar over the observation, we have already achieved a dynamic range of 40 dB compared to the sky noise. The round-off errors of the analog beamformer are still clearly visible. In future experiments, this effect can be mitigated by dithering, which will become more effective once more and more tiles are added.

E. Sensitivity Measurement on the Sun

On October 28, 2009, the first ten tiles were connected to the back-end for the first interferometric observation on the Sun. Solid engineering tests have made it possible that the Sun was already clearly detected in the first test observation. This is very reassuring in view of the system integration of even larger prototype systems and ultimately the SKA. At the end of the morning, the tiles were pointed one hour ahead of the Sun for a so called drift scan through the tile beams. In such a measurement, the weights w_k are kept fixed while the phasor of the source $\mathrm{e}^{\mathrm{j}\mathbf{k}\boldsymbol{\xi}_{pk}}$ changes due to the rotation of the Earth. Since the source moves through the beam, the sensitivity of the element beam pattern towards the source changes as well. However, the element beam pattern being considerably broader than the array factor, this is a secondary effect.

Figure 17 shows the real part of some measured cross-correlations. In radio astronomy, these variations caused by changes in the propagation delays due to Earth rotation are called fringes. These first fringes were observed by 10 tiles arranged in a 4-element uniform linear array (ULA) and a 6-element ULA, each with roughly East-West orientation. The observation was done in a single 195 kHz channel at 1179 MHz with 10 seconds integration.

The curves show the correlations of the tile at the indicated distance from the first tile of the 6-element ULA. The width of the envelope of these fringes has a size that corresponds to the beam width of a single tile, as expected. The amplitude of this envelope allows us to determine the sensitivity, expressed as the ratio of effective area A_{eff} over the system temperature T_{sys}, towards the sun at $(az, el) = (178.0°, 23.9°)$ using

$$\frac{A_{\mathrm{eff}}}{T_{\mathrm{sys}}} = \frac{2k_{\mathrm{b}}}{S_{\mathrm{sun}}} \frac{P_{\mathrm{sun}}}{P_{\mathrm{n}} + P_{\mathrm{sun}}}, \tag{18}$$

where S_{sun} is the flux of the sun, $P_{\mathrm{sun}}/\left(P_{\mathrm{n}} + P_{\mathrm{sun}}\right)$ is the ratio of the power received from the sun over the system noise power including the self-noise from the sun and $k_{\mathrm{b}} = 1.38 \cdot 10^{-23}$ $\mathrm{WK}^{-1}\mathrm{Hz}^{-1}$ is the Boltzmann constant. At the time of observation, the solar flux at 2.8 GHz was about $80 \cdot 10^{-22}$ $\mathrm{Wm}^{-2}\mathrm{Hz}^{-1}$ [36], which corresponds to $14.2 \cdot 10^{-22}$ $\mathrm{Wm}^{-2}\mathrm{Hz}^{-1}$ at 1179 MHz assuming that the Rayleigh-Jeans approximation holds for the solar radio spectrum at these frequencies.

The correlation coefficients shown in Fig. 17 are computed by dividing the power in the cross-correlation between two tiles by the square root of the product of the auto-correlations of the corresponding tiles. From this definition, it follows that the cross-correlation coefficient is directly related to the

instantaneous SNR of the sun:

$$\frac{P_{\rm sun}}{\sqrt{\left(P_{\rm n}+P_{\rm sun}\right)^2}} = \frac{P_{\rm sun}}{P_{\rm n}+P_{\rm sun}} = 0.25. \qquad (19)$$

Using (18), we thus find that the sensitivity in the direction $(az, el) = (178.0°, 23.9°)$ is $A_{\rm eff}/T_{\rm sys} = 4.86 \cdot 10^{-3}$ m^2/K.

In an infinite dense phased array, the effective area of an element can not be larger than its physical area within the array. We can use this fact to find an upper limit for the system temperature by assuming that this also holds for the tiles that are fully enclosed by other tiles in the array. The physical size of the tile is $A_{\rm phy} = 1.125$ m^2, which we have to multiply by the cosine of the zenith angle of the sun in the measurement ($66.1°$) to account for projection effects. We can thus estimate $T_{\rm sys}$ as

$$T_{\rm sys} = \frac{A_{\rm phy}\cos\left(66.1°\right)}{A_{\rm eff}/T_{\rm sys}} = 94.7 \text{ K}. \qquad (20)$$

This result is better than we expected. Since the tiles surrounding the tiles used for this experiment are not powered, the edge elements of the active tiles may pick up currents from neighboring tiles thus effectively enlarging their effective area. This implies that $A_{\rm phy}$ may be somewhat larger than the physical area of a single tile. This effect could easily increase $A_{\rm phy}$, and therefore $T_{\rm sys}$ calculated above, by 10 to 25%. This implies that the actual system temperature probably lies between 104 K and 118 K. In the future, this measurement should definitely be repeated with the full array powered on to determine the impact of this edge effect more accurately. The low elevation of the sun ($23.9°$) might be another source of error, since the EMBRACE system was only designed for scan angles up to $45°$ from zenith.

The LNA noise temperature is expected to be the dominant contribution to the overall system temperature. We may thus judge the reasonableness of our result by examining the expected LNA noise temperature $T_{\rm LNA}$, which is described by [24]

$$T_{\rm LNA} = T_{\rm min} + T_0 \frac{4r_{\rm n}\left|\Gamma_{\rm act}-\Gamma_{\rm opt}\right|^2}{\left(1-\left|\Gamma_{\rm act}\right|^2\right)\left|1+\Gamma_{\rm opt}\right|^2}. \qquad (21)$$

In this equation, $\Gamma_{\rm opt}$ is the reflection coefficient with optimal matching for minimal noise, $T_{\rm min}$ is the minimal noise temperature when the LNA is matched to $\Gamma_{\rm opt}$, $T_0 = 290$ K by definition, $\Gamma_{\rm act}$ is the active reflection coefficient, and $r_{\rm n}$ is the normalized noise resistance. Typical values for the EMBRACE LNA at 1179 MHz are $T_{\rm min} = 44$ K, $r_{\rm n} = 0.031$ and $\Gamma_{\rm opt} = -0.48$. The absolute value of the active reflection coefficient of an infinite array in the direction of the sun was obtained from a full EM-simulation in HFSS and was found to be $|\Gamma_{\rm act}| = 0.77$.

The phase of $\Gamma_{\rm act}$ is not well defined since the two reflection coefficients were obtained from two different reference planes. This implies that the value of $|\Gamma_{\rm act} - \Gamma_{\rm opt}|$ may vary from 0.29 to 1.25. In the most optimistic scenario, in which the phases of $\Gamma_{\rm act}$ and $\Gamma_{\rm opt}$ are the same, the second term in (21) may be as low as 27.5 K. This gives a total LNA noise temperature of 71.5 K. Adding a second stage contribution in the system of approximately 25 K and the sky noise contribution of 3 K, the expected minimum system noise temperature is around 100 K for this specific scan angle.

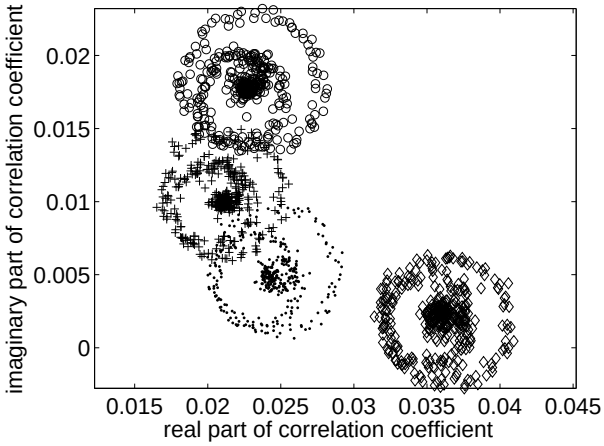

Fig. 18. Plot showing fringes of Cas A on a number of baselines in the 3×3-tile sub-array. The observation was done in a single 195 kHz frequency channel at 1278 MHz with 30 s integration per sample.

F. Observation of Cassiopeia A

Given that the accuracy of the measurement is hampered by the fact that the position of the sun was outside the scan range specification for EMBRACE and that the simulation results are difficult to interpret due to the mismatch in reference planes for the reflection coefficients, it is very reassuring that the numbers obtained from simulations and experiments are as close as they are. However, it would be be nice to confirm the sensitivity measurement with a source closer to the zenith. We therefore observed the radio source Cassiopeia A (Cas A) with the 3×3-tile sub-array. In this measurement, which started on 15 January 2010 at 17:29:11 UTC and was done at 1278 MHz, the tiles were pointed at a point 23.257° from the zenith such that Cas A would drift through the main beam of the tiles. The integration time per snapshot was 30 seconds to ensure sufficient SNR. Since the array is quite small, the fringe will only have a few periods, which hampers accurate reading of the amplitudes from a standard plot like Fig. 17. We therefore plotted the real and imaginary part of the time series centered on the transition of Cas A in Fig. 18.

This plot shows that the correlation coefficient on Cas A in the center of the main beam is about 0.6%. Based on recent flux measurements on Cas A at 1405 MHz [37], the spectrum of Cas A in the 1980.0 epoch [38] and the known frequency dependent decay of Cas A at 927 and 1405 MHz [37], we can assume that the flux of Cas A at 1278 MHz is 1955 ± 60 Jy. This results in $A_{\rm eff}/T_{\rm sys} = 8.47 \cdot 10^{-3}$ m^2/K in the direction of Cas A, which indicates a system temperature towards zenith of 123 K.

There are several effects that could explain the difference between this result and the system temperature derived from the solar measurements. Figure 18 clearly shows that all correlations have a complex valued offset, which suggests a contribution of correlated noise in the system. Since the

configuration of both the front-end and the back-end in the 3×3-tile setup differs from the setup with the two ULAs, choices like connection schemes, LO-tuning and observing frequencies can have significant impact. This is clearly a topic for further system evaluation. However, the simple fact that we were able to detect Cas A so clearly with such a limited system is reassuring for continued aperture array developments.

VI. Conclusions

In this paper we presented the design, development, manufacture and testing of EMBRACE, a phased array technology demonstrator for SKA. We also presented array factor measurements on the analog tile beamformer exploiting a novel technique that does not require calibration of the array to obtain accurate results. The first measurements on an astronomical source, the Sun, indicate that the tiles have a system temperature in the range 104 – 118 K, which is reassuringly close to the design specification of 100 K.

References

[1] P. E. Dewdney, P. J. Hall, R. T. Schilizzi, and T. J. L. W. Lazio, "The square kilometre array," *Proceedings of the IEEE*, vol. 97, no. 8, pp. 1482–1496, Aug 2009.

[2] P. N. Wilkinson, "The hydrogen array," in *IAU Colloquium 131, ASP Conference Series, Radio Interferometry: Theory, Techniques and Applications*, T. J. Cornwell and R. A. Perley, Eds., 1991, vol. 19, pp. 428–432.

[3] R. Braun, "The square kilometer array interferometer," in *The Westerbork Observatory, Continuing Adventure in Radio Astronomy*, R. Raimond and R. O. Genee, Eds. Dordrecht, The Netherlands: Kluwer, 1996, pp. 167–184.

[4] A. van Ardenne and F. Smits, "Technical aspects for the square kilometer array interferometer (SKAI)," in *Proc. High-sensitivity radio astronomy workshop*, N. Jackson and R. J. Davis, Eds., Jodrell Bank, U.K., Jan. 1996, pp. 282–286.

[5] R. Braun, "The concept of the square kilometre array interferometer," in *Proc. High-sensitivity radio astronomy workshop*, N. Jackson and R. J. Davis, Eds., Jodrell Bank, U.K., Jan. 1996, pp. 260–268.

[6] P. J. Hall, "The square kilometre array: an international engineering perspective," *Experimental Astronomy*, vol. 17, no. 1-3, pp. 5–16, 2004.

[7] R. T. Schilizzi *et al.* (2007, Dec.) Preliminary specifications for the square kilometre array. 100_Memo_Schilizzi.pdf. [Online]. Available: http://www.skatelescope.org/documents/memos/

[8] J. D. Bunton and S. G. Hay, "SKA cost model for wide field-of-view options," *Experimental Astronomy*, vol. 17, no. 1-3, pp. 381–405, 2004.

[9] J. D. Kraus, *Radio Astronomy*, 2nd ed. Powel (Ohio): Cygnus-Quasar Books, 1986.

[10] N. E. Kassim, "Towards the long wavelength array," in *Proceedings of the XXIXth General Assembly of the Internation Union of Radio Science (URSI GA)*, Chicago (Ill.), USA, 7-16 Aug. 2008.

[11] S. W. Ellingson, T. E. Clarke, A. Cohen, J. Craig, N. E. Kassim, Y. Pihlstrom, L. J. Rickard, and G. B. Taylor, "The long wavelength array," *Proceedings of the IEEE*, vol. 97, no. 8, pp. 1421–1430, Aug. 2009.

[12] J. D. Bregman, "Concept design for a low frequency array," in *SPIE Proceedings Astronomical Telescopes and Instrumentation, Radio Telescopes*, vol. 4015, 2000, pp. 19–33.

[13] M. de Vos, A. W. Gunst, and R. Nijboer, "The LOFAR telescope: System architecture and signal processing," *Proceedings of the IEEE*, vol. 97, no. 8, pp. 1431–1437, Aug. 2009.

[14] C. Lonsdale, "The murchison widefield array," in *Proceedings of the XXIXth General Assembly of the International Union of Radio Science (URSI GA)*, Chicago (Ill.), USA, 7-16 Aug. 2008.

[15] C. J. Lonsdale *et al.*, "The murchison widefield array: Design overview," *Proceedings of the IEEE*, vol. 97, no. 8, pp. 1497–1506, Aug. 2009.

[16] L. A. Baker *et al.*, "The US technology development project for the SKA," in *Proceedings of the XXIXth General Assembly of the Internation Union of Radio Science (URSI GA)*, Chicago (Ill.), USA, 7-16 Aug. 2008.

[17] G. Cortes. (2009, Apr.) QSC feed pattern measurements. Memo_2009Cortes_QSC_Feed_Pattern_Measurements.pdf. [Online]. Available: http://skatdp.astro.cornell.edu/files/

[18] G. Cortes and B. Imbriale. (2009, Aug.) SKA offset optics design. Memo_2009Cortes_OffsetOptics.pdf. [Online]. Available: http://skatdp.astro.cornell.edu/files/

[19] C. Carilli and S. Rawlings, Eds., *Science with the Square Kilometre Array*. Amsterdam, The Netherlands: Elsevier, 2004, vol. 48.

[20] D. R. DeBoer *et al.*, "Australian SKA pathfinder: A high-dynamic range wide-field of view survey telescope," *Proceedings of the IEEE*, vol. 97, no. 8, pp. 1507–1521, Aug. 2009.

[21] M. V. Ivashina, O. A. Iupikov, R. Maaskant, W. A. van Cappellen, L. Bakker, and T. A. Oosterloo, "Off-axis beam performance of focal plane arrays for the westerbork synthesis radio telescope - initial results of a prototype system," in *Antennas and Propagation Society International Symposium, 2009. APSURSI '09. IEEE*, June 2009.

[22] W. A. van Cappellen, L. Bakker, and T. A. Oosterloo, "Experimental results of a 112 element phased array feed for the westerbork synthesis radio telescope," in *Antennas and Propagation Society International Symposium, 2009. APSURSI '09. IEEE*, June 2009.

[23] A. van Ardenne, J. D. Bregman, W. A. van Cappellen, G. W. Kant, and J. G. Bij de Vaate, "Extending the field of view with phased array techniques: Results of European SKA research," *Proceedings of the IEEE*, vol. 97, no. 8, pp. 1531–1542, Aug. 2009.

[24] G. Gonzales, *Microwave Transistor Amplifiers: Analysis and Design*. Englewood Cliffs (New Jersey), USA: Prentice-Hall Inc., 1984.

[25] M. V. Ivashina, R. Maaskant, and B. Woestenburg, "Equivalent system representation to model the beam sensitivity of receiving antenna arrays," *Antennas and Wireless Propagation Letters, IEEE*, vol. 7, pp. 733–737, 2008.

[26] A. B. Smolders and G. W. Kant, "Thousand element array (THEA)," in *Antennas and Propagation Society International Symposium, 2000. IEEE*, vol. 1, 2000, pp. 162–165.

[27] D. H. Schaubert, T.-H. Chio, and H. Holter, "TSA element design for 500–1500 MHz array," in *Antennas and Propagation Society International Symposium, IEEE*, vol. 1, 2000, pp. 178–181.

[28] G. A. Hampson and J. G. bij de Vaate, "Verification of THEA tile calibration and beamforming results using a near field scanner," in *European Microwave Conference*, Oct 2001, pp. 1–4.

[29] A. O. Boryssenko and D. H. Schaubert, "Single-polarized, dielectric-free, Vivaldi tapered slot phased array: performance prediction," in *Antennas and Propagation Society International Symposium, IEEE*, vol. 2, 2001, pp. 436–439.

[30] S. J. Wijnholds, A. G. de Bruyn, J. D. Bregman, and J. G. bij de Vaate, "Hemispheric imaging of galactic neutral hydrogen with a phased array antenna system," *Experimental Astronomy*, vol. 17, no. 1-3, pp. 59–64, 2004.

[31] H. Holter and H. Steyskal, "Some experiences from FDTD analysis of infinite and finite multi-octave phased arrays," *IEEE Transactions on Antennas and Propagation*, vol. 50, no. 12, pp. 1725–1731, Dec 2002.

[32] H. Holter, T.-H. Chio, and D. H. Schaubert, "Experimental results of 144-element dual-polarized endfire tapered-slot phased arrays," *IEEE Transactions on Antennas and Propagation*, vol. 48, no. 11, pp. 1707–1718, Nov 2000.

[33] T.-H. Chio and D. H. Schaubert, "Parameter study and design of wide-band widescan dual-polarized tapered slot antenna arrays," *IEEE Transactions on Antennas and Propagation*, vol. 48, no. 6, pp. 879–886, Jun 2000.

[34] S. J. Wijnholds, J. D. Bregman, and A. J. Boonstra, "Sky noise limited snapshot imaging in the presence of RFI with LOFAR's initial test station," *Experimental Astronomy*, vol. 17, no. 1-3, pp. 35–42, 2004.

[35] S. J. Wijnholds and A. J. van der Veen, "Multisource self-calibration for sensor arrays," *IEEE Transactions on Signal Processing*, vol. 57, no. 9, pp. 3512–3522, Sep. 2009.

[36] J. Alvestad. Solar terrestrial activity report. Updated daily. [Online]. Available: www.solen.info

[37] D. E. Reichart and A. W. Stephens, "The fading of supernova remnant Cassiopeia A from 38 MHz to 16.5 GHz from 1949 to 1999 with new observations at 1405 MHz," *The Astrophysical Journal*, vol. 537, no. 2, pp. 904–908, Jul. 2000.

[38] J. W. M. Baars, R. Genzel, I. I. K. Pauliny-Toth, and A. Witzel, "The absolute spectrum of Cas A: An accurate flux density scale and a set of secondary calibrators," *Astronomy & Astrophysics*, no. 61, pp. 99–106, 1977.

PLACE
PHOTO
HERE

Stefan J. Wijnholds
(S'2006, M'2010) was born in The Netherlands in 1978. He received M.Sc. degree in Astronomy and the M.Eng. degree Applied Physics (both cum laude) from the University of Groningen in 2003. After his graduation he joined the R&D department of ASTRON, the Netherlands Institute for Radio Astronomy, in Dwingeloo, The Netherlands, where he works with the system design and integration group on the development of the next generation of radio telescopes. From 2006 to 2010 he was also affiliated with the Delft University of Technology in Delft, The Netherlands, where he received the Ph.D. degree (cum laude) in 2010. His research interests lie in the area of array signal processing, specifically calibration and imaging.